Mach 4 Testing of Scramjet Inlet Models

Takeshi Kanda,* Tomoyuki Komuro,* Goro Masuya,† Kenji Kudo,* Atsuo Murakami,*
Kouichiro Tani,* Yoshio Wakamatsu,† and Nobuo Chinzei‡
National Aerospace Laboratory, Kakuda Research Center, Miyagi, Japan

Six scramjet inlet models were tested in a Mach 4 wind tunnel. Wall and pitot pressure were measured and schlieren photographs were taken. Parameters of these models are side-plate sweep angle, contraction ratio, and cowl geometry. The shock pattern inside one of the models, as shown by schlieren photographs, coincides with the calculations. Both mass-capture ratio and total pressure recovery are 50–70%. There seems to be a better sweep angle and a better cowl length for maximum total pressure recovery.

Nomenclature

A = cross-sectional area
a = velocity of sound
h = height of the inlet
M = Mach number
m = mass flow rate
P = pressure
X = distance from upstream to downstream
Y = distance from top to bottom
Z = distance
η = efficiency

Subscripts

a = air
c = captured
t = total
w = wall
∞ = freestream

I. Introduction

THERE is great interest in the application of scramjets to engines of aerospace planes. A scramjet is composed of an inlet, a combustor, and a nozzle. The inlet has an important function: it captures and adequately compresses air in a broad range of flight Mach numbers and flight dynamic pressures with little loss of total pressure. On the other hand, there are many problems to be addressed toward the improvement of the inlet performance, especially in low flight Mach numbers. For example, unstart of the inlet is a serious problem in scramjet engine operations. The scramjet inlet has been studied in depth in the United States, both analytically and experimentally. However, there have been only a few reports that are unclassified.[1,2]

Recently, we carried out testing of various scramjet inlet models in a Mach 4 wind tunnel; schlieren photographs around and inside the model were taken, and pitot and wall pressures were measured. Mass-capture ratio and total pressure recovery of the models tested were compared. We introduce the test results here.

II. Experimental Apparatus and Inlet Model

A. Wind Tunnel

The Mach 4 wind tunnel used is shown in Fig. 1. It is an intermittent type, which has a rectangular test section 110 mm high and 100 mm wide. The transient time to establish a steady Mach 4 stream in the tunnel is about 1 s, and the total time of each run is about 13 s. This inlet entrance Mach number of 4 corresponds to a flight Mach number of about 5, because the air into the airframe-integrated scramjet already passes through the shock wave produced at the nose of the airframe. Total pressure and total temperature of the airstream in the wind tunnel are 1.6 MPa and room temperature, respectively. Inlet models are attached to the wind tunnel as shown in Fig. 1. The leading edge of each model is located 20 mm downstream from the entrance of the test section.

B. Inlet Model

The inlet models used in this test, which are based on the NASA Langley model,[1] are composed of two side plates and a cowl, but have no struts. The surface of the wind tunnel acts as the upper wall of each model. The length from the leading edge to the model throat is 110 mm in all of the models. The reference model (type A) is shown in Fig. 2a. Sweep angle and contraction ratio (entrance/throat area ratio) of the reference model are 45 deg and 5, respectively. The cowl geometry and its position on the reference model is as shown in Fig. 2a.

We used the other five models to compare the effects of sweep angle and contraction ratio as shown in Table 1.

The geometry and the length of the cowl were also chosen as test parameters as shown in Fig. 2b. Three types of cowl geometry, designated as V, M, and I, were tested for each model. Experiments with cowls attached 10 mm and 20 mm upstream of the reference cowl position were also carried out. Such cowls are designated as, e.g., V + 10 or V + 20 in this report, whereas the reference cowl is designated as V + 0 or, simply, V.

C. Measurements

Wall pressure on the side plates and on the upper wall is measured at 78 points in total. The diameter of the wall

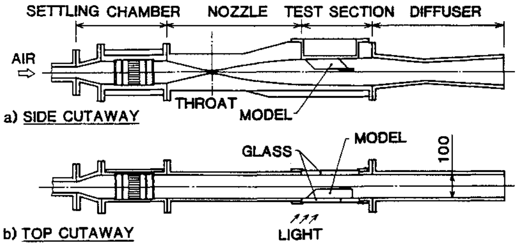

Fig. 1 Mach 4 wind tunnel.

Presented as Paper 89-2680 at the AIAA/ASME/SAE 25th Joint Propulsion Conference, Monterey, CA, July 10–12, 1989; received May 22, 1989; revision received Oct. 18, 1989.

*Researcher.

†Senior Researcher.

‡Head, Ramjet Performance Section.

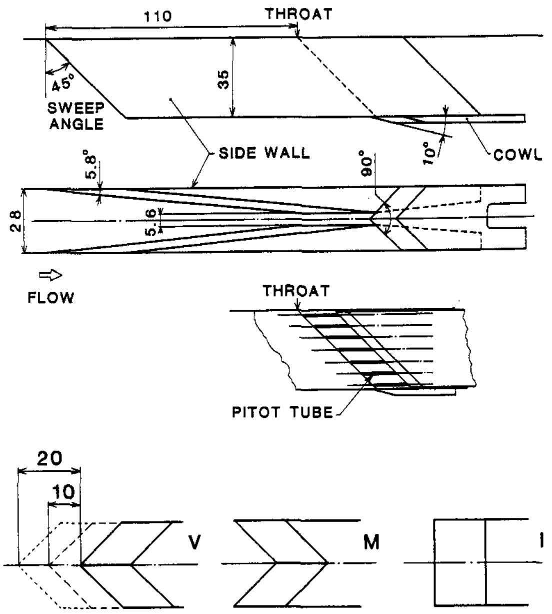

Fig. 2 Inlet model: a) reference model (type A); and b) cowl geometry.

Table 1 Inlet model

Model	A	B	C	D	E	F
Sweep angle, deg	45	60	30	0	45	45
Contraction ratio	5	5	5	5	3	7

pressure orifice is 0.5 mm. Pitot pressure at the throat section is measured by a pitot tube rake as shown in Fig. 2a. The pitot tubes are set parallel to the upper wall. The inner and the outer diameters of the pitot tubes are 0.3 mm and 0.6 mm, respectively. Response time of the pitot probe is much shorter than the running time of 13 s.

The pressure-measuring system is constructed by pressure transducers, dynamic strain meters, an A/D converter, and a microcomputer. End-to-end accuracy of the system is more than 0.995.

The flow direction inside each model is considerably downward, but we did not examine the flow direction inside or around the model. Although it is not yet confirmed how much difference there is between the flow direction and the pitot-probe direction, the error in the pitot pressure resulting from misalignment of the probe is generally small. Because we could not measure the static pressure, we employed the wall pressure in place of the static pressure at the throat assuming that the static pressure is uniform along the transverse Z direction. This may result in some error in the data reduction. We need further measurement of static pressure and flow direction to examine the order of those errors.

We took a schlieren photograph of the side view of each model. The bottom view (inside view) of type A was also photographed. For the bottom view, the model was attached to a window, and the light entered parallel to the side-plate leading edge of the model as shown in Fig. 1b.

III. Results and Discussion

A. Reference Model (Type A)

1. Flow Inside/Around Model

The inside view of the type A model is shown in Fig. 3 where a) is a schlieren photograph, b) is a calculation by shock relation, and c) is the result obtained by the two-dimensional Navier-Stokes code, NASCRIN.[3] These are the views of the plane perpendicular to the side-plate leading edge. The schlieren photograph shows good agreement with the calculated results.

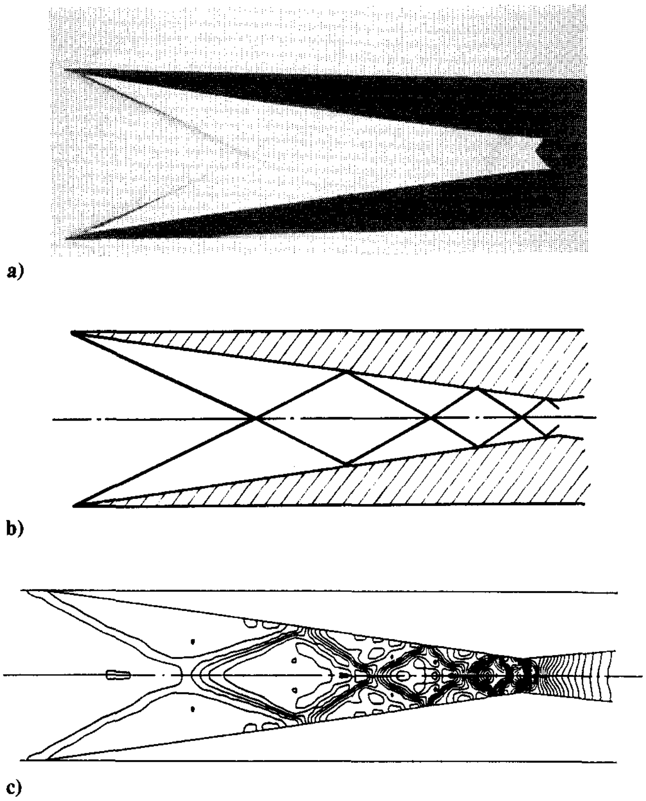

Fig. 3 Flow inside the type A model: a) schlieren photograph; b) shock relation; and c) NASCRIN (pressure).

The shock relation is convenient to determine the shock pattern or the change of pressure inside the model. If more detailed information is required, NASCRIN is useful as shown in Fig. 3. Despite good agreement between the experiment and the two-dimensional calculations we pay attention to the fact that the flow inside the model is three dimensional.

Three-dimensional phenomena cannot be calculated by the above two methods. For example, the pressure change by the shock relation is greater than the measured pressure in this test. This seems due to the interferences of the shock wave from the side-plate leading edge with other waves; e.g., 1) the expansion wave on the upper wall; 2) the shock waves which originate at the cowl; and 3) the expansion waves at the bottom of the side plate. Detailed information cannot be obtained using the shock relation. The three-dimensional code is necessary to clarify the understanding of the flowfield around or inside the model.

The schlieren photograph of the side view around the model is shown in Fig. 4. The boundary-layer part of the upper plate is indicated by B.L. in the figure. The boundary-layer thickness of 99% of the freestream velocity is 10 mm at 90 mm from the entrance of the test section.

Because of the downward flow from the inside of the model, a vortex is seen to start at the bottom end of the side-plate leading edge to grow gradually, and to change its direction twice discontinuously between the leading edge and the cowl. (This portion of the photograph was, at first, considered as a shear layer. A three-dimensional Navier-Stokes simulation calculated by Ishiguro et al.[4] clearly showed that it represents a pair of vortices rolling up at the bottom of the side plates.) Even when the cowl was removed, the flow direction change occurred. Therefore, the change has no relation to the cowl. Because of the downward flow inside the model, the expansion wave can be seen to propagate from the leading edge of the cowl.

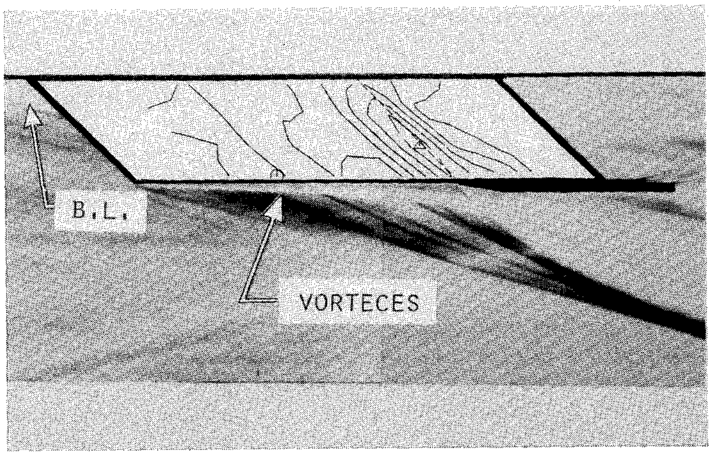

Fig. 4 Side view and side-wall pressure of type A.

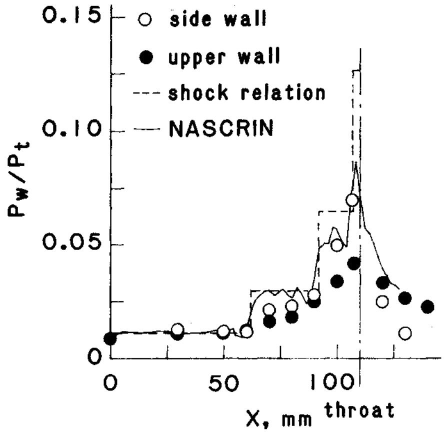

Fig. 5 Centerline pressure distributions on side and upper walls of type A.

Several weak shock waves can be seen between the leading edge and the cowl. The starting positions of these weak shock lines in Fig. 4 coincide with positions where two shock waves cross or where a shock wave reflects on the side wall as shown in Fig. 3.

Behind the shock waves, the pressure becomes higher and the flow direction becomes more downward. The vortex between the freestream and the downward flow from the model changes its flow direction after the shock waves. Therefore the weak shock lines seen in the side view seem to arise as a result of this flow direction change of the vortex.

2. Wall Pressure

The wall pressure contour on the side plate of the type A model is also shown in Fig. 4 with an interval of $(P_w/P_t) = 0.01$ starting at $P_w/P_t = 0.01$. The wall pressure becomes higher near the throat and between the cowl and the centerline of the side wall. Distribution of P_w/P_t along the centerline of the side wall and of the upper wall is shown in Fig. 5, with results calculated by shock relation and by NASCRIN. The measured side-wall pressure roughly coincides with the results by shock relation and by NASCRIN. There is no stepwise change at the upper wall pressure in contrast to the side wall. Perhaps this is the result of expansion waves that spread on the upper wall.

3. Mach Number and Total Pressure Recovery

The distributions of Mach number and total pressure at the throat section of type A are shown in Fig. 6. They are deduced from the pitot pressure and the wall pressure. The Mach number becomes larger near the cowl than near the upper wall, while the total pressure becomes larger between the cowl and the centerline. Because the total temperature is uniform in the test section, the mass flow rate at the throat is calculated from these distributions. The mass capture ratio m_c/m_∞ and the mean total pressure recovery η_{pt} are 73 and 72%, respectively. These factors are defined as follows:

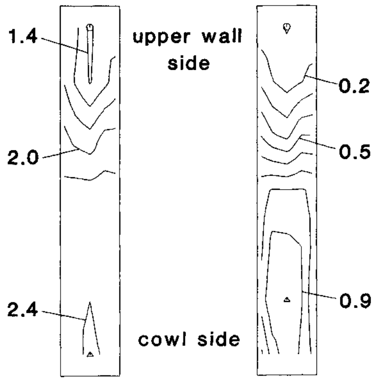

a) Mach No. b) $P_{t,local}/P_t$

Fig. 6 Mach number and total pressure at the throat of type A.

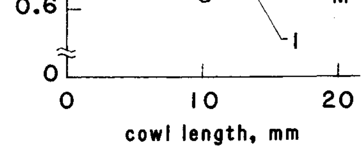

Fig. 7 Effect of cowl geometry and length (type A).

$$\left(\frac{m_c}{m_\infty}\right) = \frac{\text{Mass flow rate at the throat}}{\text{Mass flow rate at the entrance of the inlet}}$$

$$\eta_{pt} = \frac{\text{Mass-weighted mean } P_t \text{ at the throat}}{P_t \text{ of the freestream}}$$

In the evaluation of m_∞, the boundary layer at the entrance of the model is considered. These values roughly agree with

NASA's results,[5,6] which reported a mass-capture ratio of 75% and a total pressure recovery of 80%, respectively. The mass-capture ratio by NASCRIN is 78%.

B. Effect of Cowl Geometry and Length

The mass-capture ratio and the total pressure recovery for each type of cowl are shown in Fig. 7 with cowl length. Type V shows the best performance in total pressure recovery, but there is little difference in the mass-capture ratio among three cowl geometries. Although not shown here, Mach number distribution with type I is less symmetrical than that with the other cowls.

It should be noted that the total pressure recovery is worst with the 10-mm cowl length in each geometry. The mass-capture ratio increases with cowl length. The extended cowl blocks the downward flow, and the shock wave seems to originate from the cowl. Large total pressure loss, therefore, is caused by the extended cowl. This shock wave causes significantly nonuniform flow at the entrance of the combustor and boundary-layer separation.

C. Effect of Side-Plate Leading-Edge Sweep Angle

Four models with different sweep angle of the side-plate leading edge were tested, among which unswept model of type D did not start. Here, we discuss the result of models which started, and that of type D will be discussed later.

In type B, shown in Fig. 8, and type C, the vortices under the side walls are deflected twice between the leading edge and the cowl as in type A. The vortex direction changes of type A occur at about 60 and 90 mm from the leading edge, while those of type B occur at about 50 and 75 mm and those of type C occur at about 65 and 95 mm.

Compared with type A, the wall pressure of type B is lower while that of type C is higher. Therefore, the level of the wall pressure increases with decrease of the sweep angle.

The largest Mach number at the throat is about 2.5 in each model. The distributions of Mach number and total pressure at the throat of type B are similar to those of type A. In comparison with these, the distributions of Mach number and of total pressure of type C are more complicated (see Fig. 9).

Effects of the sweep angle on the mass-capture ratio and the total pressure recovery are shown in Fig. 10. Within the range of the present test conditions, there is an optimal sweep angle around 45 deg.

The incoming flow changes its direction downward due to the swept shock waves produced by the side plate, which reduces the velocity component perpendicular to the leading edge. When the sweep angle is large, e.g., in type B, the downward velocity component is large, so there is a great deal of spillage.

The total pressure recovery becomes worse when the sweep angle is large. This results because a large part of the incoming flow, which has a high total pressure, is spilled; whereas the flow near the upper wall, which has a low total pressure, is not spilled. The mean total pressure, therefore, is low.

The total pressure recovery also becomes worse when the sweep angle is small, i.e., in type C. The reason may result from the stronger shock waves from the side-plate leading edge. However, because the difference of total pressure recovery from that of type A is small, we could not clearly determine the reason.

D. Effect of Contraction Ratio

The vortex direction changes in type E occur at about 65 and 100 mm from the leading edge, while those in type F occur at about 60 and 80 mm.

Of the Mach numbers in all models, that at the throat of type E is highest. The distribution of Mach numbers and that of total pressures at the throat of type E are rather complicated and are far from uniform. The distributions at the

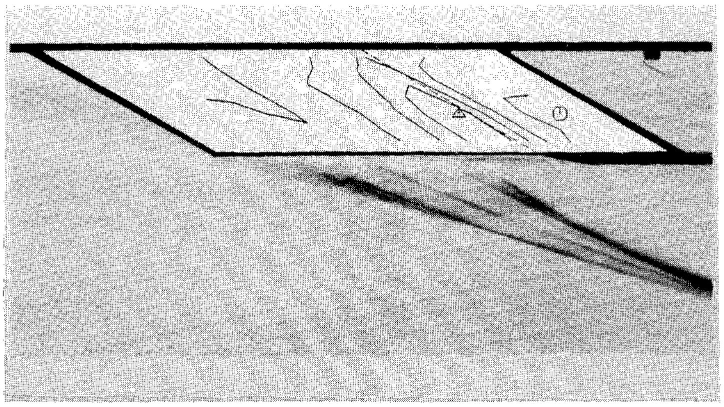

Fig. 8 Side view of type B.

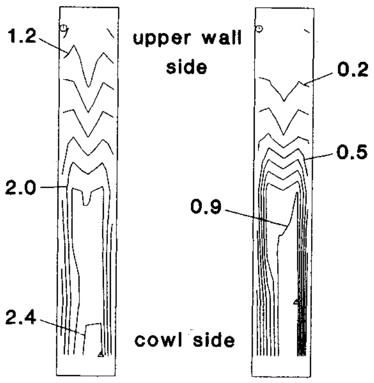

a) Mach No. b) $P_{t,local}/P_t$

Fig. 9 Mach number and total pressure at the throat of type C.

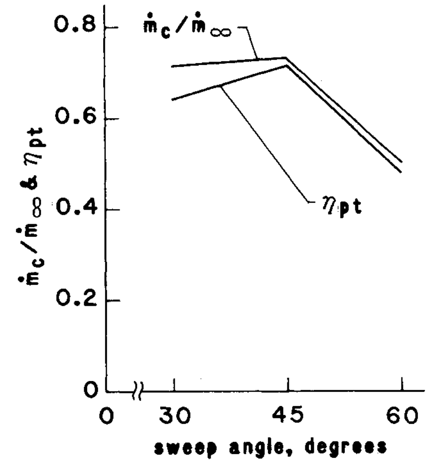

Fig. 10 Effect of side-plate leading-edge sweep angle.

throat of type F are simple, while the Mach numbers are lower than that of type A. Comparing the three models, the mass-capture ratio and the total pressure recovery become lower as the contraction ratio increases as shown in Fig. 11.

When the contraction ratio is large, e.g., in type F, the wedge angle of the side plate is large. Therefore, the flow with higher density is changed more downward.

The reason for higher total pressure recovery in the lower contraction model is because of a smaller number and weaker strength of the shock waves due to a smaller wedge angle. Compression of the lower contraction model, however, is less than that of the higher contraction model.

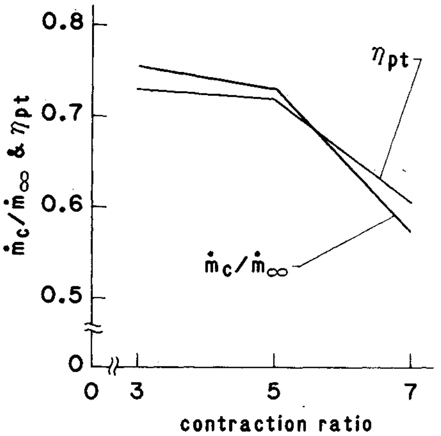

Fig. 11 Effect of contraction ratio.

E. Unstart Phenomena

As mentioned before, type D with any geometry and length of the cowl did not start even without the pitot rake. Type C with V + 20 cowl did not start either when the pitot rake was attached to the model. The Kantrowitz-Donaldson's maximum allowable contraction ratio[7] to start supersonic decelerating duct flow is about 1.5 for Mach 4. This value is much smaller than those of the present models. Spillage from the unclosed lower surface is found to be very important to start the models.

When the model does not start, i.e., the flow at the throat is not supersonic, both the mass-capture ratio and the total pressure recovery become much smaller than those of the model which starts, e.g., type A, as shown in Table 2. Side view and wall-pressure distribution for the start case are compared with those for the unstart case in Fig. 12. The lowest value of the P_w/P_t contour for the unstart case is 0.02, whereas that for the start case is 0.01.

The photograph indicates that the strong shock originates not in front of the model but inside the model. The shock waves of the unstart case are unclear in comparison with those of the start case.

The side-wall pressures along the centerline of the two cases are shown in Fig. 13. Stepwise change can be seen in the start

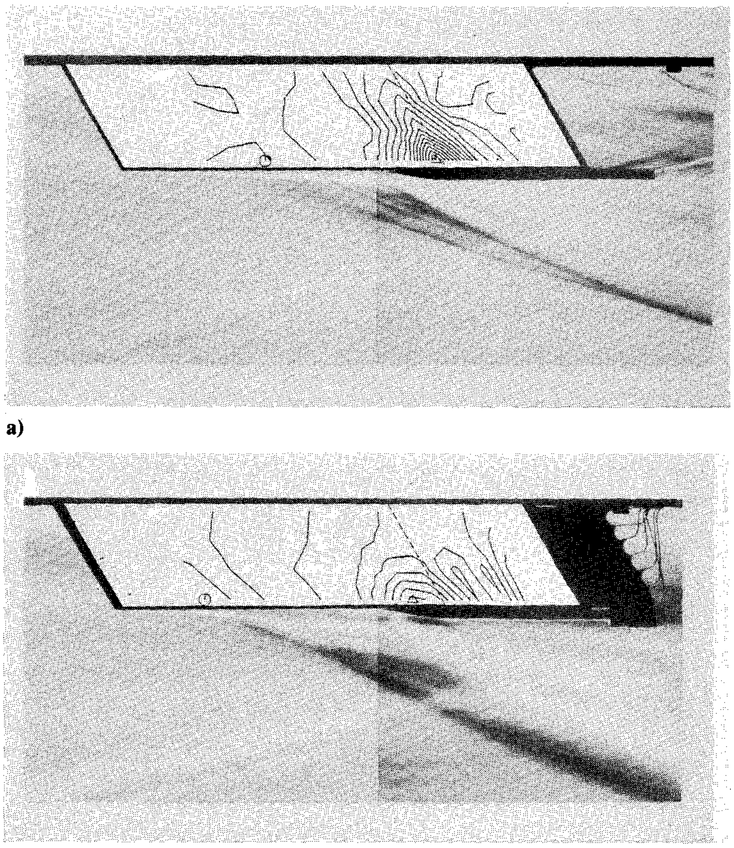

a)

b)

Fig. 12 Side view of type C with V + 20 cowl: a) start; and b) unstart (with pitot probe).

Table 2 Performance comparison between a start case and an unstart case

Model	A(V + 0)	C(V + 20)	D(V + 0)	D(V + 10)	D(V + 20)
Start/unstart	Start	Unstart	Unstart	Unstart	Unstart
Mass-capture ratio	0.73	0.25	0.33	0.27	0.26
Total pressure recovery	0.72	0.17	0.21	0.15	0.14

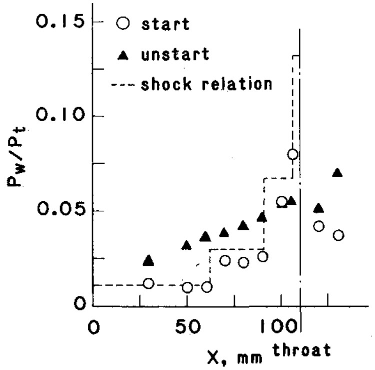

Fig. 13 Side-wall pressure of type C with V + 20 cowl.

case, whereas change is gradual in the unstart case.

In the unstart case, the average pressure inside the model is higher than that in the start case, because a shock wave produced in the starting period could not be swallowed through the throat. As a result, more air inside the model flows downward from the model as a result of this high pressure, making the mass-capture ratio very small. The mechanism for the total pressure loss in the unstart case is similar to that in the start cases, but its intensity is much higher.

Spillage drag is estimated as follows: the dividing streamline, which separates air entering the combustor from that spilling, is straight, and change of the transversely averaged pressure along it is linear. For the models with contraction ratio of 5, spillage drag coefficient based on the freestream dynamic pressure and the projected area of the model entrance is 0.03–0.09 for the start cases and 0.10–0.13 for the unstart cases. Large spillage and high static pressure in the unstart cases result in high spillage drag coefficient.

IV. Conclusions

We carried out testing of scramjet inlet models in a Mach 4 wind tunnel, taking schlieren photographs, as well as measuring wall and pitot pressures. The following points have been clarified by the present test.

1) The shock pattern inside the model is confirmed by the schlieren photographs.

2) Both the shock relation and a two-dimensional computation code, such as NASCRIN, are useful in determining the flow inside the model. However, a three-dimensional computation code is necessary to clarify the flow inside the model.

3) There is a little difference in performance by cowl geometry, although length of the cowl influences mass-capture ratio and total pressure recovery. The shortest cowl shows the highest total pressure recovery and the lowest mass-capture ratio.

4) The model with a sweep angle of 45 deg has the highest total pressure recovery within the range of this test.

5) The small-contraction-ratio model has the best total pressure recovery and the highest mass-capture ratio but with the weakest compression.

6) The small-sweep-angle model tends not to start. In the unstart case, both total pressure recovery and mass-capture ratio become significantly lower than those in the start case.

The static pressure and the flow direction must be measured to get better results, although we know that this is a difficult task. Tests at other Mach numbers are necessary to investigate the influence of a Mach number on the inlet model performance.

Acknowledgment

The authors acknowledge the useful assistance of Munekazu Mochizuki, the National Aerospace Laboratory, Kakuda Research Center.

References

[1] Trexler, C. A., and Souders, S. W., "Design and Performance at a Local Mach Number of 6 of an Inlet for an Integrated Scramjet Concept," NASA TN D-7944, Aug. 1975.

[2] Kumar, A., "Numerical Simulation of Scramjet Inlet Flow Fields," NASA TP-2517, May 1986.

[3] Kumar, A., "User's Guide for NASCRIN—A Vectorized Code for Calculating Two-Dimensional Supersonic Internal Flow Fields," NASA TM-85708, Feb. 1984.

[4] Ishiguro, T., Ogawa, S., and Wada, Y., "Numerical Computation of Flow for Scramjet," *Proceedings of the 7th NAL Symposium on Aircraft Computational Aerodynamics*, National Aerospace Lab., Tokyo, NAL SP-10, Nov. 1989, pp. 99–104 (in Japanese).

[5] Trexler, C. A., "Inlet Performance of the Integrated Langley Scramjet Module," AIAA Paper 75-1212, Sept. 1975.

[6] Waltrup, P. J., Anderson, G. Y., and Stull, F.D., "Supersonic Combustion Ramjet (Scramjet) Engine Development in the United States," *Proceedings of the 3rd International Symposium on Air Breathing Engines*, DGLR-Fachbuch, Cologne, Germany, No. 6, March 1976, pp. 836–862.

[7] Crocco, L., "One-Dimensional Treatment of Steady Gas Dynamics," *Fundamentals of Gas Dynamics*, edited by H. W. Emmons, Princeton Univ. Press, Princeton, NJ, 1958, pp. 184–190.